Article:
Ghimire, B., Kumar, S., Lamichhane, P. et al. (2026) Atmospheric-pressure plasma jet interacting with saline and non-saline medium: plasma characteristics & liquid-phase chemistry. Journal of Physics D: Applied Physics, 59 (24). 245201. ISSN: 0022-3727

https://doi.org/10.1088/1361-6463/ae7124

Atmospheric-pressure plasma jet interacting with saline and non-saline medium: plasma characteristics & liquid-phase chemistry

Journal of Physics D: Applied Physics

OPEN ACCESS

RECEIVED
1 February 2026

REVISED
29 April 2026

ACCEPTED FOR PUBLICATION
21 May 2026

PUBLISHED
15 June 2026

PAPER

Atmospheric-pressure plasma jet interacting with saline and non-saline medium: plasma characteristics & liquid-phase chemistry

Bhagirath Ghimire[1,2,3,4,*], Sushil K K C[5], Pradeep Lamichhane[3,6], Nishtha Gaur[4], Jun-Seok Oh[7], Kunning G Xu[2], Endre J Szili[8], Robert D Short[4,9] and Eun Ha Choi[3]

[1] Center for Space Plasma and Aeronomic Research, The University of Alabama in Huntsville, Huntsville, AL 35899, United States of America
[2] Department of Mechanical and Aerospace Engineering, The University of Alabama in Huntsville, Huntsville, AL 35899, United States of America
[3] Department of Electrical and Biological Physics, Kwangwoon University, 20 Kwangwoon-ro, Nowon-Gu, Seoul 01897, Republic of Korea
[4] Department of Chemistry and Material Science Institute, Lancaster University, Lancaster, LA1 4YW, United Kingdom
[5] University of South Australia, Mawson Lakes Campus, Adelaide, South Australia 5095, Australia
[6] Department of Chemical Engineering, Imperial College London, South Kensington SW7 2AZ, United Kingdom
[7] Graduate School of Engineering, Osaka Metropolitan University, Osaka 599-8531, Japan
[8] 30 Joann Street Athelstone, South Australia 5076, Australia
[9] School of Mathematical and Physical Sciences, Dainton Building, 13 Brook Hill, Sheffield S3 7H, United Kingdom
[*] Author to whom any correspondence should be addressed.

E-mail: ghimirebhagi@hotmail.com

Keywords: plasma jet, plasma medicine, cold plasma, plasma–liquid interaction, optical emission spectroscopy, plasma diagnostics

Abstract

The application of atmospheric-pressure plasma jets (APPJs) in medicine often involves interaction with saline environments. This study examines how the salinity of the target liquid influences APPJ behaviour and plasma-induced liquid chemistry. The APPJ is used to treat two types of targets: (a) deionized water (DIW) and (b) an agarose gel made in DIW, with both targets made with and without the inclusion of physiologically-relevant 150 mM NaCl. APPJ is operated with argon gas at an applied voltage of 1.60 kV (rms), current of 1.95 mA (rms), frequency of ≈35kHz, and output power of ≈0.55W. The coupling of the APPJ with the DIW or NaCl solution establishes a stronger conductive path for the flow of current/charge towards the target. The magnitude of charge/current flow is higher for the 150 mM NaCl solution due to the presence of more conductive ions inside the solution. The higher flow of charges towards NaCl solution leads to a stronger emission from excited species at the plasma–liquid interface and this is confirmed through optical emission spectroscopy. It was found that the APPJ produced more hydrogen peroxide (H_2O_2) and nitrites (NO_2^-), as markers of reactive oxygen and nitrogen species, respectively, in DIW compared to 150 mM NaCl. However, the oxidation potential of agarose gel was qualitatively enhanced with the addition of NaCl. These contrasting results suggest that measurement of H_2O_2 and NO_2^- is not reliable to predict the oxidative potential of all media, particularly with saline media. We attribute the discrepancy in our result to the formation of potent oxidant hypochlorous acid (HOCl) in saline media, which inhibits the formation of H_2O_2 as described in the manuscript through the differing chemical reaction pathways that take place when the APPJ interacts with DIW and NaCl solution, and their respective rate coefficients.

1. Introduction

Atmospheric-pressure plasma jets (APPJs) have attracted significant attention over the past two decades due to their ability to generate non-thermal plasmas that can be safely operated in open air and brought into direct contact with liquids and soft matter [1–3]. These sources produce a rich mixture of energetic electrons, ions, excited species, ultraviolet (UV) radiation, and reactive oxygen and nitrogen species

(RONS), making them highly attractive for applications ranging from surface treatment and materials processing to environmental remediation and plasma-based medicine [4–6]. Among these, biomedical applications such as wound healing, sterilization, cancer therapy, and blood coagulation have emerged as particularly promising areas for APPJ deployment [7, 8].

A defining feature of plasma in medicine is the unavoidable interaction with liquid environments as biological tissues and fluids are predominantly aqueous and contain dissolved electrolytes [6, 9]. As a result, plasma–liquid interactions play a central role in determining the transport, transformation, and lifetime of plasma-generated reactive species [10, 11]. Numerous studies have demonstrated that long-lived species such as hydrogen peroxide (H_2O_2), nitrite (NO_2^-), nitrate (NO_3^-), and changes in pH act as key chemical mediators linking plasma exposure to biological responses [12, 13]. However, most fundamental plasma–liquid studies have traditionally relied on distilled or deionized water (DIW) as the target medium, which does not adequately represent the electrolyte-rich conditions encountered in real biomedical environments.

Liquid conductivity and ionic composition can significantly influence both plasma behavior and plasma-induced liquid chemistry. In saline media, the presence of ions such as Na^+ and Cl^- modifies the electrical boundary conditions at the plasma–liquid interface, potentially affecting discharge current, electric field distribution, and power coupling [14]. At the same time, chloride-containing solutions introduce additional chemical pathways, including the formation of chlorine-based oxidants such as hypochlorous acid (HOCl), which are absent in pure water but are highly relevant in biological systems [15]. Despite their importance, the combined effects of salinity on APPJ discharge characteristics and reactive species generation remain insufficiently understood.

To establish a clearer link between plasma physics and liquid-phase chemistry, it is essential to investigate plasma–liquid interactions using well-controlled diagnostics while systematically varying liquid properties. Several prior studies have investigated the characteristics of the APPJ or dielectric barrier discharge (DBD) in contact with saline or phosphate-buffered saline [14]. Baik *et al* investigated the effect of feeding gas composition (air vs N_2) in four different physiological solutions (DIW, 0.9% NaCl, phosphate buffered saline—PBS, and Dulbecco Modified Eagle's medium) on the decontamination of *Escherichia coli* [16]. While the results are useful to compare decontamination effects, the underlying chemistry and characteristics of the plasma jets in contact with different physiological solutions was not investigated. Nie *et al* investigated the effects of tissue thickness and liquid composition on the penetration depth of RONS using a He+O_2 APPJ [17]. Their study investigated the concentration of RONS into six different types of liquids (double distilled water, 1% PBS, 0.9% NaCl, 5% glucose, 2% serum and 10% serum solution) below the pig muscle tissue. Whilst their study provides important information about the fate of long-lived RONS at different depths, the underlying characteristics of the APPJ as well as liquid solution(s) and the underlying plasma chemistry was not investigated. Zhao *et al* investigated the effect of the fluid environment on the inactivation efficiency of plasma activated water (PAW) and plasma activated—PBS against *Pseudomonas fluorescens* [18]. The results from this study demonstrated stronger decontamination efficacy of PAW but the underlying mechanisms were not investigated. Jirasek and Lukes presented important results on the oxidation of saline by a μ-APPJ operating with He/O_2 gas flow [15]. Their study indicated the role of hypochlorite ion or HOCl for the strong oxidation of the saline medium with the APPJ. The observations from these findings are very useful to understand the interaction of APPJ with saline medium but more studies are required to advance the field for safe and efficient application in medicine.

In this work, an argon APPJ is employed to treat two representative liquids: distilled water and an aqueous 150 mM NaCl solution. 150 mM NaCl solution was chosen as it represents concentration of sodium salts typically found in physiological fluids. The characteristics of the APPJ are analyzed using electrical and optical diagnostics, while the chemistry of the liquid after plasma treatment is analyzed through absorbance spectroscopy, measurement of long-lived RONS (H_2O_2, NO_2^-), and pH. To further bridge the gap between simplified liquid models and biologically relevant conditions, a KI-starch gel system is used to visualize plasma-generated reactive species under saline and non-saline conditions. By correlating plasma behavior, liquid chemistry, and visual indicators of oxidative activity, this study provides new insight into how target liquid salinity governs plasma–liquid interactions, with direct relevance to plasma–tissue interactions in plasma biomedical applications.

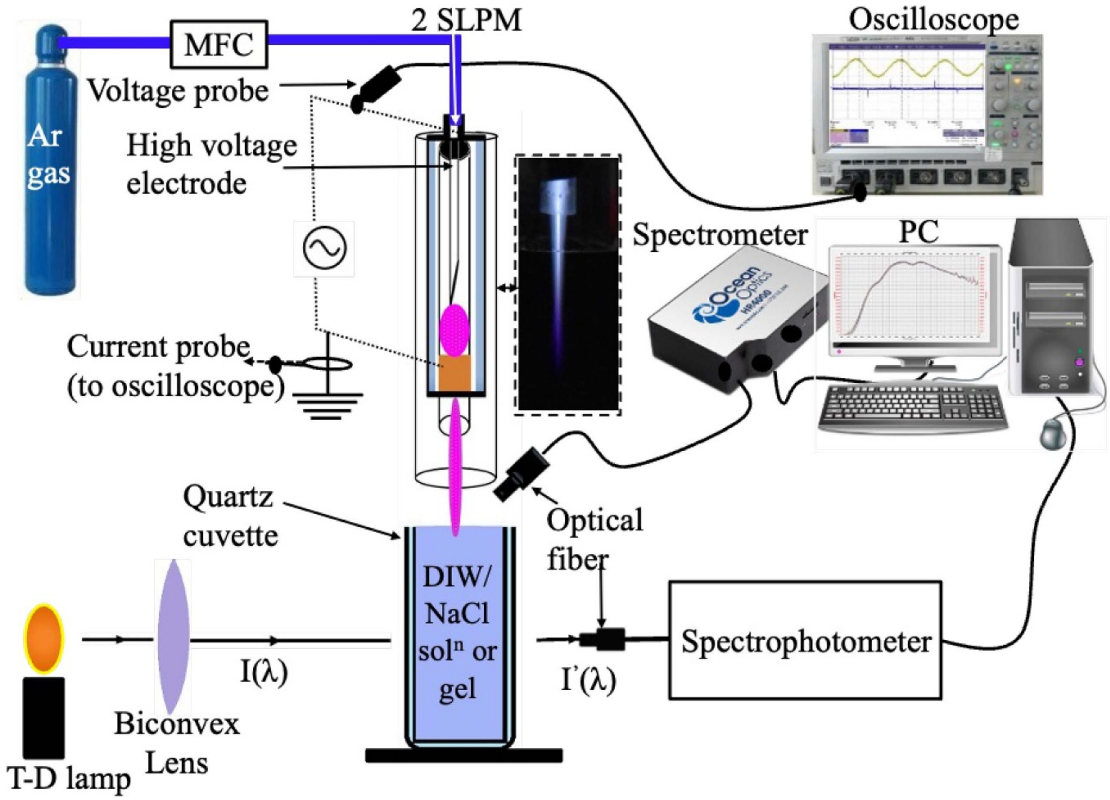

Figure 1. Schematic of the experimental setup.

2. Experimental setup and methodology

2.1. Setup of the APPJ to treat saline and non-saline medium

Figure 1 is a schematic of the experimental setup. An APPJ is designed by inserting a stainless-steel needle electrode (diameter 1.2 mm) with pointed tip inside a quartz tube (inner diameter (ID): 2 mm, outer diameter (OD): 4 mm). This needle electrode acts as the high voltage (HV) electrode. The ground electrode is made up of copper (thickness 0.5 mm, width 5 mm) and this this is wrapped outside the quartz tube at 10 mm below the tip of the HV electrode. The jet configuration is then inserted inside a stainless steel tubing (ID 5 mm, OD 8 mm) which is isolated from the HV electrode but in contact with the ground electrode. This is then inserted inside the quartz tube (ID = 10 mm, OD = 12 mm) for safety. The distance from the end of the inner quartz tube to the end of the outer quartz tube was 8 mm. Operation of the APPJ is done using a custon-built power supply (frequency ≈35 kHz) which produces sinusoidal waveforms when operated with a direct current power supply [22]. Argon gas with a purity of 99.99% was fed through the HV electrode at a constant flow rate of 2 standard liters per minute (SLPM), and its flow rate was controlled using a mass flow controller (MFC).

A transparent quartz cuvette (internal volume: 4.5 ml) was placed at 4 mm position below the external quartz tube and it was filled with two types of targets (liquid or gel). In one set of experiments, the quartz cuvette was filled with: (a) DIW, conductivity ≈0.5 μS cm^{-1}, and (b) sodium chloride (NaCl) solution with a concentration of 150 mM, conductivity ≈15 mS cm^{-1} and subjected to 5 min of plasma treatment. Analysis of the liquid characteristics were then done by measuring long-lived RONS (H_2O_2 and NO_2^-), pH and liquid absorbance. Optical emission spectra (OES) of the APPJ in contact with two liquid targets was also conducted. In another set of experiments, the quartz cuvette was filled with potassium iodide (KI)-starch solution or KI-starch agarose gel made using (a) DIW and (b) 150 mM NaCl solution. Absorbance of the KI-starch solution as well as visualization of the color changes of the gel after 5 min of plasma treatment were conducted afterwards in order to investigate the effects induced by argon APPJ into the saline or non-saline target. No significant deformation of the liquid or gel surface was observed at the chosen gas flow rate of 2 SLPM used in this study.

2.2. Measurement of electrical signals

Voltage (V) and current (I) waveforms of the discharge were recorded using a HV probe (Model P6015A, Tektronix) and current probe (Model P6022, Tetronix), and were recorded in an oscilloscope (Lecroy Wavesurfer 434, 350 MHZ). In order to obtain the charge (Q)–voltage (V) Lissajous plots, a 4.7 nF capacitor was connected in series with the ground electrode and a passive voltage probe (10:1) was connected across it. All signals were averaged 512 times in order to reduce the effect of noise.

2.3. Optical emission spectroscopy

OES of the discharge were collected by using a spectrometer (Model HR4000+CG-UV-NIR, Ocean Insights Inc.) equipped with an optical fiber of diameter 600 μm. The optical fiber was placed at an angle of 45° above the liquid target (see figure 1) at ≈1.5 cm away from the plasma–liquid interface. The intensities were calibrated to absolute values ($\mu W/cm^2$ nm) using a deuterium (D)–halogen (T) light source (S/N: 089370012, Ocean Insights Inc.). OES were also collected using a monochromator (Dongwoo Optron, Monora500i) in the same configuration for a freestream APPJ and were utilized for calculating rotational temperature.

2.4. UV absorption spectroscopy (UV–Vis)

The technique of UV–Vis was used to obtain the absorbance spectra before and after plasma treatment of DIW and 150 mM NaCl solution. The emission from a Tungsten-deuterium (T-D) lamp (power: 30 W, spectral range 160–800 nm) were focused inside the quartz cuvette containing saline or non-saline media using a biconvex lens (focal length: 30 cm), and the signals were collected using an optical fiber of OD: 600 μm. The signals were then processed by a spectrometer (Model HR4000+CG-UV-NIR, Ocean Insights Inc.). Absorbance (Abs(λ)) of the plasma treated saline or non-saline medium at a particular wavelength λ) was calculated using Beer–Lambert's law as [19]:

$$\mathrm{Abs}\,(\lambda) = \log_{10}\left(\frac{I'(\lambda)}{I(\lambda)}\right) \tag{1}$$

where $I'(\lambda)$ is the transmitted light intensity and $I(\lambda)$ is the reference lamp intensity.

2.5. Measurement of H_2O_2, NO_2^-, and pH

Determination of the concentrations of H_2O_2 and NO_2^- before and after plasma treatment of the DIW and 150 mM NaCl solution were performed through colorimetric measurements. A quantiChrom^{TM} Peroxidase Assay Kit (BioAssay Systems) was used for the quantification of H_2O_2. This assay uses H_2O_2 and an electron donor dye that forms resorufin during the peroxidase reaction. The fluorescence intensity ($\lambda_{ex}/\lambda_{em} = 585$ nm/530 nm) is proportional to the concentration of H_2O_2 in the sample and this was measured using a microplate reader (BioTek Gen5). The concentrations of H_2O_2 in untreated/-plasma treated DIW or NaCl solutions were determined from the calibration curves constructed with known concentration of H_2O_2 following manufacturer's instructions [20].

Measurement of the concentrations of NO_2^- before and after plasma treatment of DIW and 150 mM NaCl solution were conducted using quantiChrom^{TM} Nitric Oxide Assay Kit (BioAssay Systems). A calibration curve was constructed with known concentration of sodium nitrite ($NaNO_2$) and measuring the fluorescence at 540 nm using a microplate reader (BioTek Gen5) following manufacturer's instructions [21]. The calibration curve was then used to estimate the concentration of NO_2^-.

Measurement of the pH of the saline and non-saline medium before and after plasma treatment was conducted by immersing a calibrated pH meter into the respective liquid solutions and values were recorded.

2.6. Visualization of the color change induced by APPJ generated RONS

A KI-starch is commonly used to visualize the formation of RONS. The principle is based upon RONS oxidizing iodide ions with the starch to produce a stable, brown colored complex [22]. Firstly, a KI-starch-agarose solution was made by heating and dissolving 0.3% KI, 0.5% starch and 0.5% agarose in (a) DIW and (b) 150 mM NaCl. The solution was then transferred to a transparent cuvette (volume: 4.5 ml) before it solidified. The solidified gel was treated by argon APPJ for 5 min and the color change of the gel immediately after plasma treatment was photographed. Absorbance spectra were also recorded in the range of 200–650 nm by treating 0.3% KI and 0.5% starch made in (a) DIW and (b) 150 mM NaCl immediately after 5 min of APPJ treatment. The spectra were recorded using the T–D lamp and a spectrometer (Model HR4000+CG-UV-NIR, Ocean Insights Inc.).

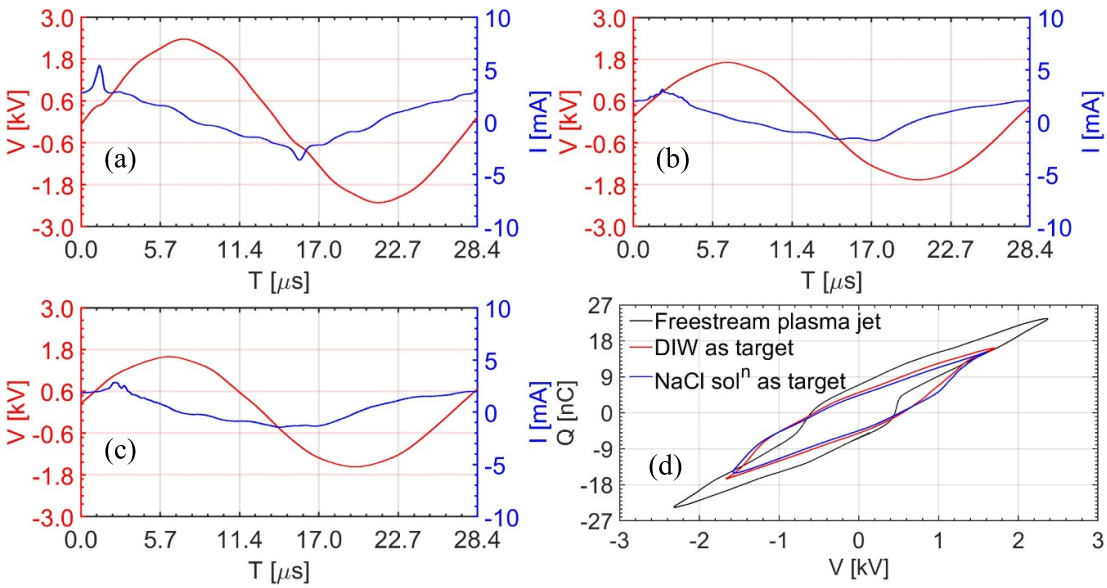

Figure 2. Electrical characteristics showing—$I-V$ waveforms of the APPJ during: (a) freestream operation, (b) contact with DIW, and (c) contact with 150 mM NaCl solution; and (d) $Q-V$ Lissajous plots for the freestream APPJ, and APPJ in contact with DIW and 150 mM NaCl solution. The current shown in figures (a)–(d) represents the total current flowing through the ground electrode of the APPJ. Each signal represents an average of 512 oscilloscope acquisitions.

3. Results and discussion

The results in this paper are presented to illustrate how the characteristics of an APPJ operating at fixed input parameters change while the APPJ comes in contact with saline and non-saline medium, and how this influences the chemistry of the target. We then use a KI-starch-agarose gel to visualize the color change during this process. The saline solution is formulated to replicate the salt levels naturally found in physiological fluids.

3.1. Electrical characteristics

The electrical characteristics ($I-V$ waveforms and $Q-V$ Lissajous plots) of the Ar APPJ operating at fixed input parameters freestream, in contact with DIW and in contact with 150 mM Nacl solution are presented in figures 2(a)–(d). The APPJ is operated at a constant frequency of ≈35.77 kHz. In all three conditions, the positive half cycle of the applied voltage is characterized by the appearance of the positive current peak while the negative part of the applied voltage is characterized by a negative current peak, typical for DBD discharges. For a freestream APPJ (no target), the average root mean square (rms) values of the voltage and current are 1.60 kV and 1.93 mA respectively. Both voltage and current values were reduced by ≈25%–26% when the target was replaced by DIW. The use of conductive target (150 mM NaCl) below the APPJ further reduced the average rms values of voltage and current by ≈5% and ≈10% respectively. Also, the observations from $Q-V$ plot (figure 2(d)) showed a similar decreasing trend in the the maximum accumulated charges for a freestream jet, jet contacting DIW and jet contacting NaCl solution. The values of maximum accumulated charges for a freestream jet, jet contacting DIW and jet contacting NaCl solution are 11.20 nC, 7.67 nC and 7.11 nC respectively. The $I-V$ waveforms (figure 2(a)–(c)) and $Q-V$ plots (figure 2(d)) measured over one period (T) were used to calculate the dissipated power.

Dissipated power (P_{I-V}) using $I-V$ waveforms was calculated as:

$$P_{I-V} = \frac{1}{T}\int_{t=0}^{t=T} I(t)\,V(t)\,\mathrm{d}t \tag{2}$$

where $I(t)$ is the total current and $V(t)$ is the applied voltage. Similarly, dissipated power (P_{Q-V}) using $Q-V$ plots was calculated as:

$$P_{Q-V} = \frac{1}{T}\int \mathrm{Q}\mathrm{d}V \tag{3}$$

Table 1. Summary of the operating parameters of the freestream Ar APPJ, and the APPJ in contact with DIW or 150 mM NaCl solution. $I-V$ waveforms ($n=3$), each averaged over 512 cycles were used to calculate the mean and standard deviation.

Condition	V_{rms} [kV]	I_{rms} [mA]	F [kHz]	P_{I-V} [W]	Q_{max} [nC]	P_{Q-V} [W]
Freestream	1.590±0.034	1.928±0.041	35.77	0.542±0.0164	11.168±0.008	0.532±0.024
DIW	1.191±0.002	1.416±0.001	35.77	0.395±0.003	7.664±0.013	0.389±0.013
NaCl	1.125±0.004	1.282±0.007	35.77	0.369±0.005	7.114±0.015	0.365±0.018

Table 2. Estimated values of discharge current, transferred charge and dissipated power along the target for the APPJ interacting with DIW and 150 mM NaCl solution. $I-V$ waveforms ($n=3$), each averaged over 512 cycles were used to calculate the mean and standard deviation.

Target type	Current [mA]	Transferred charge [nC]	Dissipated power [W]
DIW	0.512±0.001	3.503±0.013	0.146±0.003
NaCl	0.647±0.007	4.053±0.015	0.172±0.005

where Q is the charge measured across a 4.7 nF capacitor using a passive probe. A summary of the Ar APPJ operating parameters is presented in table 1. The dissipated power was the highest when the APPJ was operated freestream. The values for the APPJ contacting DIW and 150 mM NaCl solution were lower by ≈27% and ≈32%. The average dissipated power calculated using equations (2) and (3) are in close agreement validating the accuracy of our measurements.

In an APPJ, the electrical characteristics depend strongly on how the plasma couples to the downstream medium that acts as the electrical load. When the jet operates freestream, no physical target is present and the current must close through the surrounding air primarily via displacement (capacitive) currents. This weak coupling requires a higher electric field to sustain ionization, resulting in the highest measured voltage, current, and dissipated power. When the plasma impinges on a liquid target, an additional pathway of current is established through the plasma–liquid interface. This redistribution modifies the effective impedance of the system and reduces the current measured through the ground electrode of the APPJ as clearly seen in table 1.

The observations in table 1 can be used to estimate the current flowing onto the target (ΔI) as:

$$\Delta I = I_{\text{freestream}} - I_{\text{target}} \tag{4}$$

where $I_{\text{freestream}}$ is the current measured through the ground electrode of the APPJ during freestream operation, and I_{target} is the current measured through the ground electrode of the APPJ when it interacts with either DIW or with the 150 mM NaCl solution. Using equation (4), the current flowing onto the DIW and NaCl solution targets are 0.51 mA and 0.65 mA respectively. Similarly, the observations in table 1 can be used to estimate the net charge transferred to the sample ΔQ) as:

$$\Delta Q = Q_{\text{freestream}} - Q_{\text{target}} \tag{5}$$

where $Q_{\text{freestream}}$ is the maximum accumulated charges measured through the ground electrode of the APPJ during freestream operation, and Q_{target} is the maximum accumulated charges measured through the ground electrode of the APPJ when it interacts with either DIW or with the 150 mM NaCl solution. Using equation (5), the net charges transferred to the DIW and NaCl solution targets are 3.50 nC and 4.05 nC respectively.

The estimated values of discharge current, transferred charge and the dissipated power induced by the particular target (DIW or 150 mM NaCl) are summarized in table 2. During interaction of the APPJ with the 150 mM NaCl solution, a stronger conductive path is established with the target due to the presence of conductive ions which leads to higher transferred charge, higher discharge current and also higher dissipated power through the target.

In addition to sodium salts, physiological fluids also contain potassium and calcium salts. It is thus critical to understand how the characteristics of the APPJ change when it interacts with mixed salts. We tested this in a mixed salt solution containing 50 mM NaCl, 50 mM KCl and 50 mM $CaCl_2$ (conductivity ≈27 mS cm^{-1}). Analysis of $I-V$ waveforms and $Q-V$ Lissajous plots (figure 3) show that the electrical characteristics are very similar to that of the APPJ interacting with the 150 mM NaCl solution (figure 2). The measured voltage (V_{rms}), current (I_{rms}) and dissipated power derived from the $I-V$ waveforms (figure 3(a)) are observed to be 1.122±0.006 kV, 1.273±0.006 mA and 0.363±0.002 W respectively, and are very close to the ones presented in table 1. Similarly the $Q-V$ plots for the APPJ

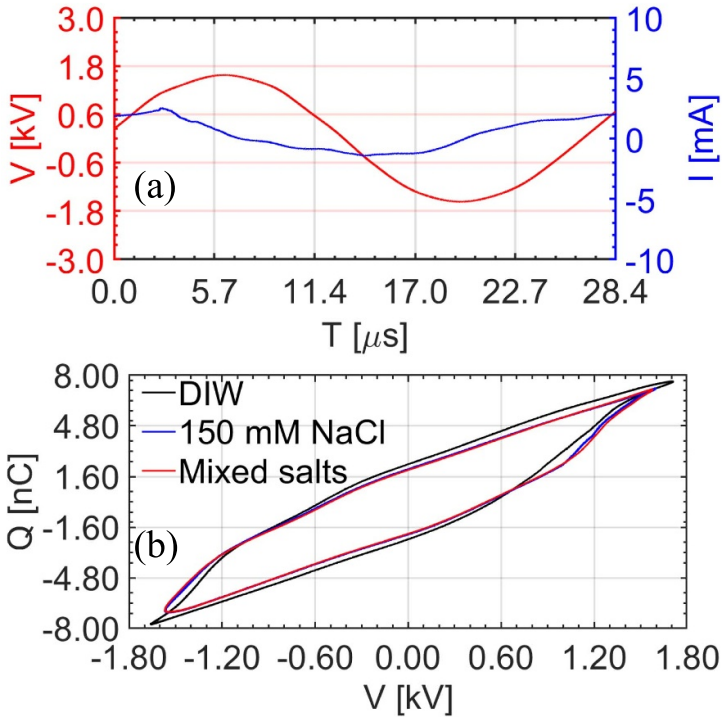

Figure 3. (a) $I-V$ waveforms of the APPJ interacting with a mixed salts solution prepared in DIW (50 mM NaCl + 50 mM KCl + 50 mM $CaCl_2$, conductivity: ≈ 27 mS cm^{-1}); (b) comparison of $Q-V$ Lissajous plots for the APPJ interacting with DIW, 150 mM NaCl and mixed salts solution (50 mM NaCl, 50 mM KCl and 50 mM $CaCl_2$). All signals were measured through the ground electrode of the APPJ. Each signal represents an average of 512 oscilloscope acquisitions.

interacting with the 150 mM NaCl solution and the mixed salts solution almost overlap (figure 3(b)), presumably due to the presence of sufficient conductive ions inside the solution.

3.2. Optical emission spectra (OES)

Optical emission characteristics of the discharge for the freestream APPJ, and the APPJ in contact with DIW and 150 mM NaCl solution are presented in figures 4(a), (b), and (c) respectively. The optical emission intensities are displayed in the unit of μW cm^{-2} nm^{-1} through calibration with a tungsten–halogen lamp. In all cases, it can be seen that the emission in the UV range of 200–400 nm is dominated by excited nitrogen species (N_2 SPS). The emissions from N_2 SPS are dominant at 315 nm, 337 nm, 356 nm and 380 nm. Emission from hydroxyl radical (OH) is also observed at 309 nm. In the visible and infrared range, emissions from excited argon species (696 nm, 706 nm, 727 nm, 738 nm, 750 nm, 763 nm, 772 nm, 794 nm, 801 nm, 810 nm, 826 nm, 842 nm, 852 nm, 866 nm) are dominant. Emission from atomic oxygen is also observed at 777 nm [23–26]. In figure 4, the absolute irradiance is highest during contact with 150 mM NaCl, surpassing the values measured for DIW contact and freestream operation. The higher emission intensity with NaCl target is ascribed to the enhancement of the discharge with the conductive ions present within the liquid solution. The conductive target promotes higher electron density and stronger localized electric field leading to higher values of absolute irradiance from excited species. This reasoning is supported by higher current and charge flow towards the target as discussed in section 3.1.

3.3. Measurement of rotational temperature

The rotational temperature of the APPJ was measured by collecting the OES with a high resolution spectrometer. This was only conducted for the APPJ operating freestream. The experimentally collected spectra from N_2 SPS at 337 nm was fitted with the simulated spectra using MASSIVEOES [27–29]. The result of fitting is shown in figure 5(a). The rotational temperature of the plasma jet is obtained to be 305.36 K. A photograph of the plasma jet touching human finger is also shown (figure 5(b)). The temperature of the treated liquid solutions also remained close room temperature. Based on our previous work, a negligible amount of evaporation of the liquid solution (≈5%–10%) is expected for the parameters used in this study; however, this was not measured.

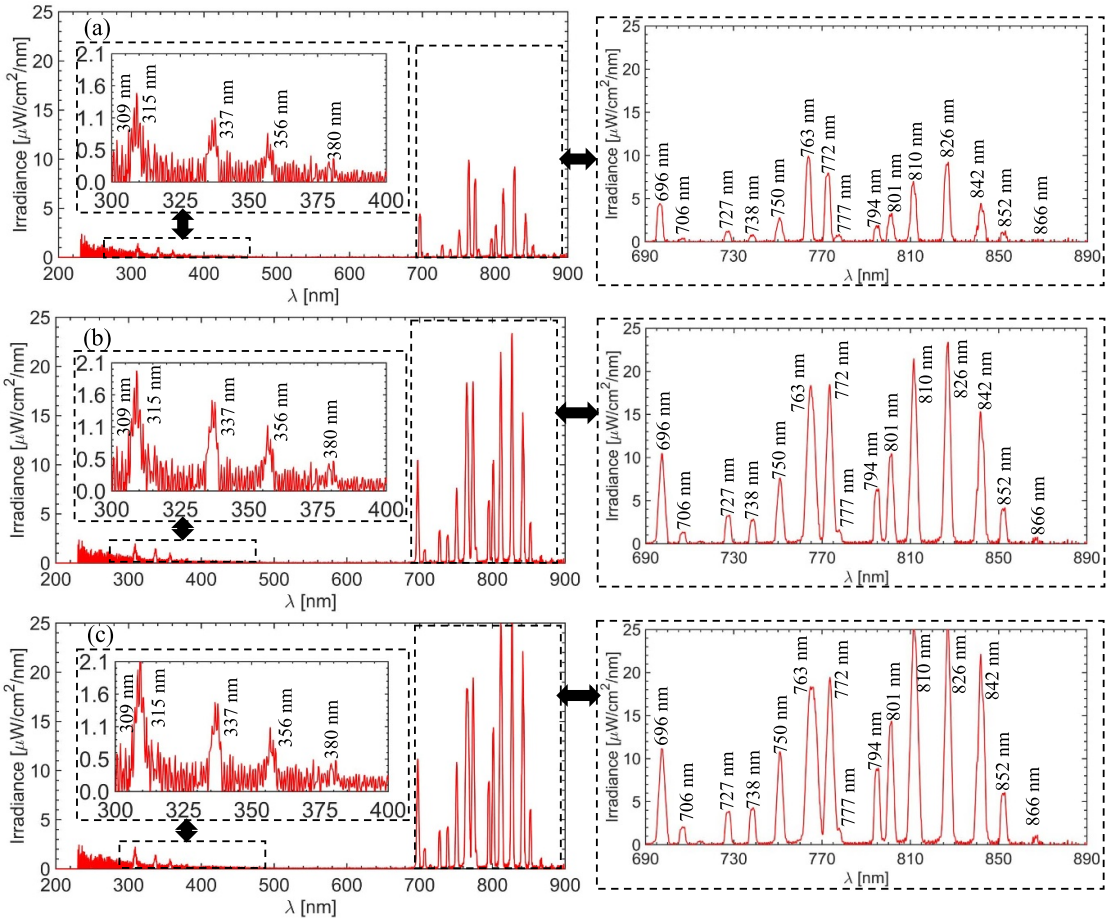

Figure 4. Optical emission characteristics of the APPJ during: (a) freestream operation; (b) contact with DIW, and (c) contact with 150 mM NaCl solution. All spectra were collected at an integration time of 100 ms with an averaging of 10.

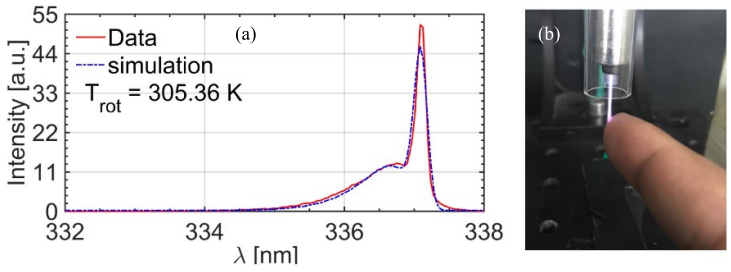

Figure 5. Determination of the gas temperature of the freestream Ar APPJ: (a) fit of experimental and simulated spectra of the N_2 SPS band at 337 nm using MASSIVEOES; and (b) photograph highlighting the safe interaction between the discharge and human tissue.

3.4. Liquid absorbance

Liquid absorbance describes the wavelength-dependent attenuation of incident UV radiation as it propagates through a liquid medium, arising from interactions between photons and dissolved molecular or ionic species. Consequently, absorbance spectra serve as a sensitive, non-intrusive probe of changes in liquid-phase chemistry induced by APPJ exposure. The absorbance spectra (obtained through Beer–Lambert's law, see equation (1)) for the APPJ contacting DIW and 150 mM NaCl solution are presented in figure 6. In the range of 200–250 nm, there is a clear separation between the two treatment conditions, indicating an increased presence of UV absorbing species in the liquid. This spectral difference is attributed to the higher accumulation/formation of long-lived RONS including H_2O_2, NO_2^-, NO_3^-, etc in plasma treated solutions and will be confirmed through colorimetric measurements in the following section.

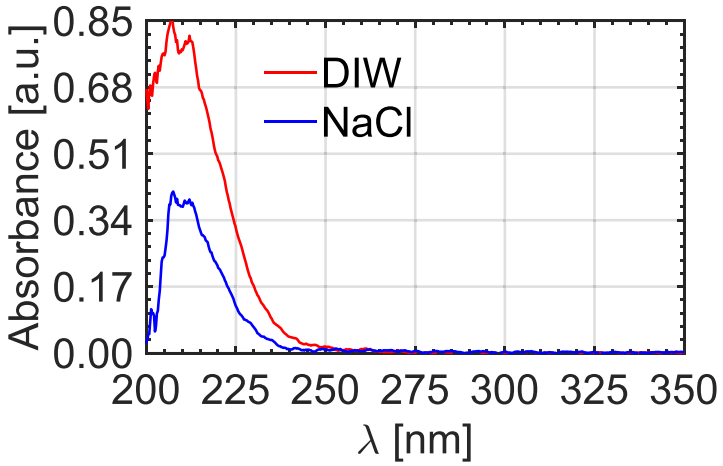

Figure 6. Absorbance spectra of APPJ treated DIW and 150 mM NaCl solution in the range of 200–350 nm. Plasma exposure time is 5 min.

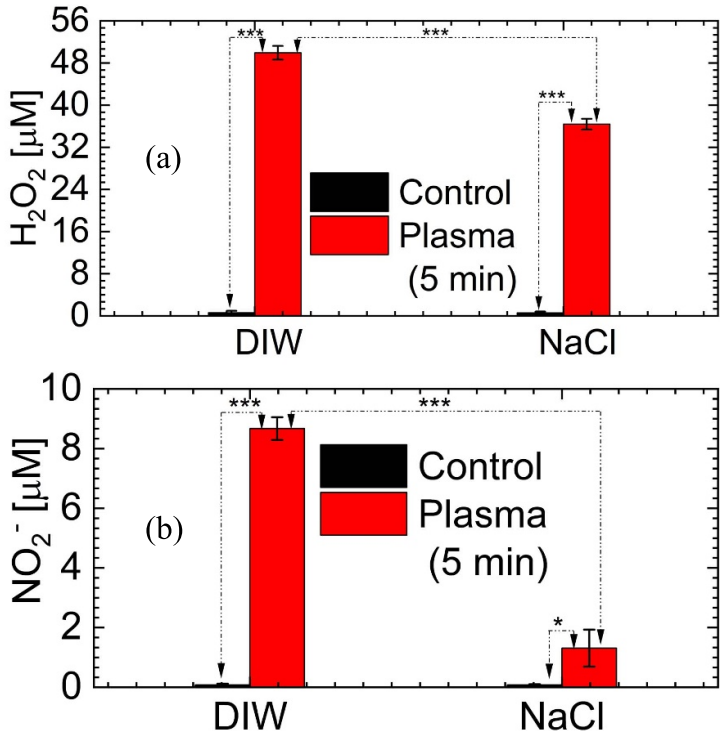

Figure 7. Measurement of (a) H_2O_2 and (b) NO_2^- concentrations from DIW and 150 mM NaCl solution treated by an argon APPJ. Plasma exposure time was 5 min. Error bars represent the standard deviation of three independent measurement ($n = 3$). Statistical significance was determined using a two-tailed, unequal variance t-test; symbols indicate significance levels: $*p < 0.05$ and $***p < 0.001$.

3.5. Measurement of RONS (H_2O_2, NO_2^-) concentrations and pH

RONS generated during plasma–liquid interactions are key mediators of the chemical and biological effects observed in APPJ treatments. Among different RONS, H_2O_2 and NO_2^- are widely used as representative markers of oxidative and nitrosative chemistry, respectively, owing to their relative stability in aqueous solutions and their accumulation as more stable products derived from short-lived, highly reactive plasma radicals. Quantifying H_2O_2 and NO_2^- therefore provides an effective and integrative means of assessing plasma-induced liquid chemistry. The concentrations of H_2O_2 and NO_2^- for the Ar APPJ contacting DIW and 150 mM NaCl solution are presented in figures 7(a) and (b), respectively. The results show that with the similar operating conditions, APPJ treatment of DIW results in higher concentration of both H_2O_2 and NO_2^-. The H_2O_2 concentration in the plasma treated DIW (49.94 μm) was

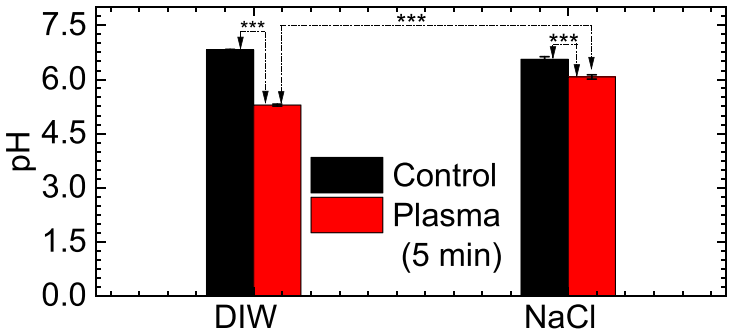

Figure 8. pH measurements of DIW and 150 mM NaCl solution treated by an Ar APPJ. Plasma exposure time was 5 min. The error bars represent the standard deviation of three independent measurements. Significant differences between groups are indicated by asterisks ($***p < 0.001$).

1.36 times higher than that in the plasma treated NaCl solution (36.71 μm). Similarly, the concentration of NO_2^- in the plasma treated DIW (8.50 μm) was 6.49 times higher than that in the plasma treated NaCl solution (1.31 μm). The higher concentrations of both H_2O_2 and NO_2^- observed in figure 7 provide explanation for higher absorbance observed with plasma treated DIW in figure 6. Observations in figure 7 also indicate that the short-lived RONS (such as hydroxyl radicals and nitric oxide) could be significantly consumed by NaCl or the H_2O_2 and NO_2^- are converted to a different product. This will be analyzed through the measurement of absorbance spectra in the UV and visible wavelength range in section 3.6.

The pH of a solution reflects its proton concentration and provides insight into the chemical environment of the liquid. During APPJ treatment, reactive species interact with water and dissolved ions, generating acidic or basic products that can shift the solution's pH. Tracking these pH changes thus offers a straightforward and sensitive approach to evaluate plasma-induced chemical transformations and to compare the effects of different treatment conditions on the liquid phase. The pH of untreated and 5 min APPJ treated solutions (DIW, 150 mM NaCl) are shown in figure 8. APPJ treatment of both DIW and 150 mM NaCl solutions results in a pH decrease. However, the final pH was lower for the DIW than NaCl solution. The final value of pH for the DIW and 150 mM NaCl solution were 5.29 and 6.07, respectively.

3.6. Visualization of the color changes induced by plasma jet generated RONS

In the next step, we visualized the color changes induced by the Ar APPJ during interaction with saline and non-saline targets. A KI-starch-agarose gel made with and without NaCl was used for this study. This methodology has been described in section 2.6. The top and side view photographs for untreated and 5 min Ar APPJ treated gels for both cases are shown in figure 9. Photograph of the argon APPJ treating KI-starch-agarose gel is also shown. Photographs were recorded immediately after plasma treatment. The top view photographs in figure 9 clearly show that the intensity of color change is much stronger when the target contains dissolved NaCl. The differences observed from the side view were minimal. These results show that salinity enhances the oxidation potential of the media but does not impact the penetration of UV photons. The increased oxidation potential of the media by NaCl is likely due to the formation of another more potent reactive species (in addition to H_2O_2 and NO_2^-) and will be explained through the various chemical reaction pathways in the following paragraphs.

The stronger color change of the KI-Starch-agarose gel made with NaCl solution in figure 9 suggests that there are additional species (besides H_2O_2 and NO_2^-) formed within the target. In order to get a better understanding of this process, we measured absorbance spectra of 5 min APPJ treated KI-starch solution with and without NaCl. The absorbance curves are presented in figure 10. Plasma treated DIW exhibits higher absorbance in the UV range (200–400 nm) (as also observed in figure 6). Beyond UV range (>400 nm and <650 nm), the absorbance from the APPJ treated NaCl solution is stronger. The observations in figures 9 and 10 suggest that the species inducing stronger color change within the NaCl dissolved KI-starch-agarose gel should be responsible for causing higher absorbance in the KI-starch-Nacl solution. This is discussed below.

In APPJs, several processes govern the formation of H_2O_2 and NO_2^-. Formation of H_2O_2 takes place through the dissociation of water vapor molecules present within the feed gas or those present at the plasma–liquid interface. These water vapor molecules can be dissociated into the highly reactive $^{\bullet}OH$

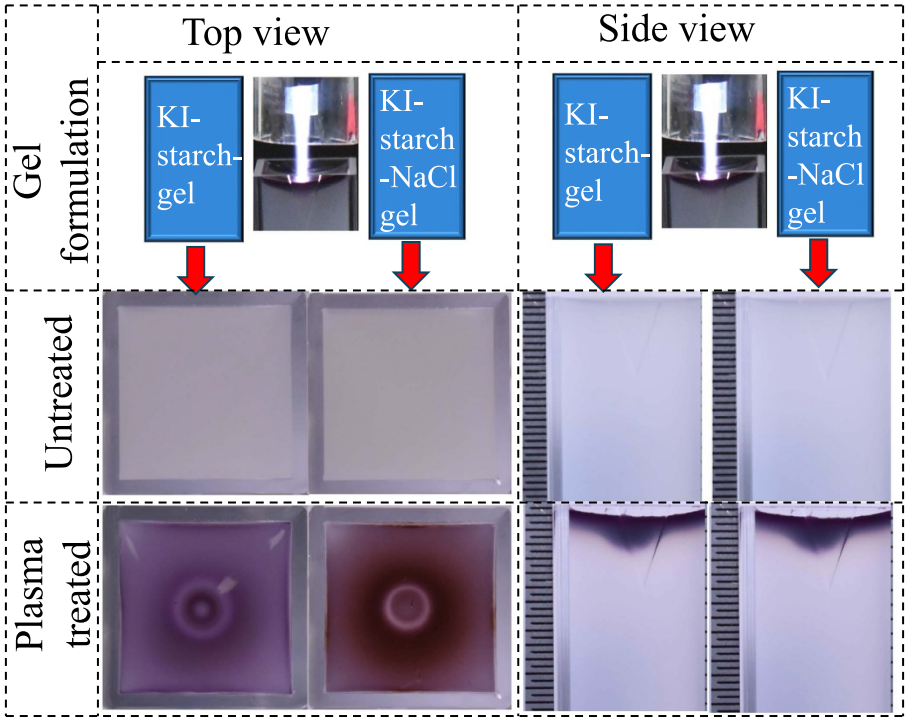

Figure 9. Photographs of the KI-starch-agarose gels (top and side views) after 5 min of APPJ treatment. The gel is made either in non-saline (DIW) or saline (150 mM NaCl) medium.

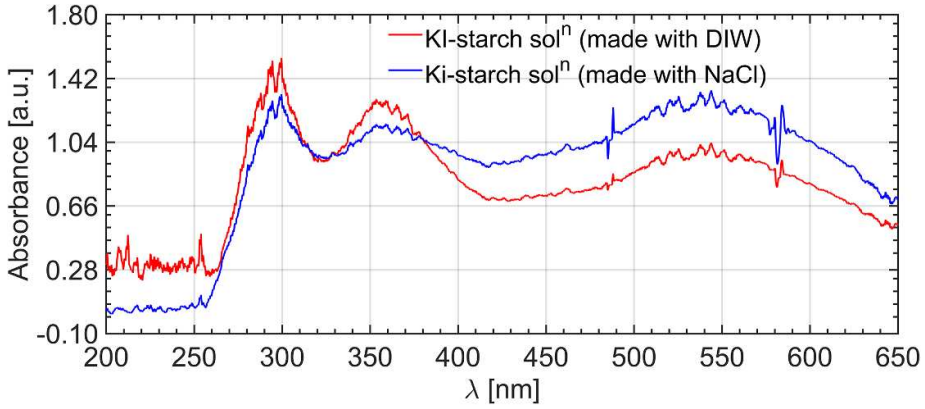

Figure 10. Absorbance spectra (200–650 nm) of KI-starch solutions with and without NaCl after 5 min of Ar APPJ treatment. Plasma exposure time was 5 min. The absorbance spectra were collected at an integration time of 50 ms with an averaging of 30.

through collisions with energetic electrons inside or outside of the quartz tube of the APPJ assembly through the following reactions [19, 23, 30–32]:

(1) $e^- + H_2O \rightarrow {}^\bullet H + {}^\bullet OH + e^-, k(\frac{E}{N})$

Excited and metastable Ar, oxygen or nitrogen atoms formed through collisions with electrons also combine with water molecules to form the $^\bullet$OH through the following reactions [19, 23, 30–32]:

(2) $e^- + Ar \rightarrow Ar_m + e^-$, $Ar_m + H_2O \rightarrow {}^\bullet OH + {}^\bullet H + Ar$

(3) $e^- + O_2 \rightarrow O(^3P) + O(^1D) + e^-$, $O(^1D) + H_2O \rightarrow 2{}^\bullet OH$ $(k = 2.2 \times 10^{-10} cm^3\ s^{-1})$

(4) $e^- + N_2 \rightarrow N_2(A^3\sum_u^+) + e^-$, $N_2(A^3\sum_u^+) + H_2O \rightarrow {}^\bullet OH + N_2 + {}^\bullet H$.

Reactions (1) and (2) occur inside and outside of the quartz tube while reactions (3) and (4) are dominant outside of the quartz tube. Our observations from optical emission spectroscopy (figure 4)

provides evidence on the formation of $^{\bullet}OH$ at the plasma–liquid interface. Additional formation of $^{\bullet}OH$ takes place through plasma-initiated UV photolysis [22, 33]:

(5) $UV + H_2O \rightarrow H_2O^*$; $UV + H_2O^* \rightarrow H^+ + OH^-$; $OH^- \rightarrow {}^{\bullet}OH + e^-$

The $^{\bullet}OH$ formed through reactions (1), (2), (3), (4) and (5) has a relatively short half-life (few hundred of nanoseconds to few microseconds) [33], and they eventually recombine to form H_2O_2 through the following reaction [19, 34]:

(6) $^{\bullet}OH + {}^{\bullet}OH \rightarrow H_2O_2$ $(k(g) = 1.78 \times 10^{-11} cm^3\ s^{-1}, k(aq) = 4.0 \times 10^9 M^{-1} s^{-1})$.

Similarly, initiation of NO_2^- in APPJs takes place through the dissociation of oxygen or nitrogen molecules and their recombination at the plasma–liquid interface as [2, 8, 32, 34, 35]:

(7) $e^- + N_2 \rightarrow N + N + e^-$

(8) $e^- + O_2 \rightarrow O + O + e^-$

(9) $N + O_2 \rightarrow NO + O$

(10) $N + {}^{\bullet}OH \rightarrow NO + {}^{\bullet}H$ $(k(g) = 5 \times 10^{-11} cm^3\ s^{-1})$

(11) $N + O \rightarrow NO$.

NO formed in reactions (9)–(11) finally recombines with O_2 and H_2O to form NO_2^- as:

(12) $4NO + 2O_2 + 2H_2O \rightarrow NO_2^- + 4H^+$ $(k(aq) = 1.0 \times 10^{10} M^{-1} s^{-1})$.

NO_2^- or HNO_2 formed during the process can also combine with H_2O_2 to form NO_3^- or ONOOH through reaction (13) and (14), which might slightly decrease the concentration of H_2O_2 in the liquid phase post plasma treatment [35, 36].

(13) $NO_2^- + H_2O_2 + H^+ \rightarrow NO_3^- + H_2O + H^+$

(14) $HNO_2 + H_2O_2 \rightarrow ONOOH + H_2O$.

Reactions (1)–(12) described above are responsible for the formation of H_2O_2 and NO_2^- in both APPJ treated DIW and APPJ treated NaCl (figures 7(a) and (b)). However, when the target solution is NaCl, the intermediate products in reactions (1)–(12) (mainly $^{\bullet}OH$ and O) participate to react with Cl^- ions resulting in the formation of HOCl through reactions (15)–(19) described below [15, 37]:

(15) $^{\bullet}OH + Cl^- \rightarrow HOCl^-$ $(k(aq) = 4.3 \times 10^9 M^{-1} s^{-1})$; $HOCl^- + H^+ \rightarrow Cl^{\bullet} + H_2O$ $(k(aq) = 2.1 \times 10^{10} M^{-1} s^{-1})$; $Cl^{\bullet} + Cl^- \rightarrow Cl_2^-$ $(k(aq) = 7.8 \times 10^9 M^{-1} s^{-1})$

(16) $Cl_2^-\bullet + {}^{\bullet}OH \rightarrow HOCl + Cl^-$ $(k(aq) = 4.5 \times 10^7 M^{-1} s^{-1})$

(17) $O + Cl^- \rightarrow OCl^-$

(18) $O + OCl^- \rightarrow ClO_2^-$

(19) $O + OCl^- \rightarrow Cl^- + O_2$.

In reactions (1)–(19), it can be seen that it is $^{\bullet}OH$ which contributes mainly to the formation of both H_2O_2 and HOCl. However, the rate coefficient that contribute to the formation of HOCl $k(aq) = 4.3 \times 10^9 M^{-1}\ s^{-1})$ is higher than the one that contribute to the formation of H_2O_2 $k(aq) = 4.0 \times 10^9 M^{-1}\ s^{-1})$. This results in the higher consumption of $^{\bullet}OH$ by chloride ions and less $^{\bullet}OH$ remains to recombine into H_2O_2. Because of this, the formation of H_2O_2 via $^{\bullet}OH + {}^{\bullet}OH \rightarrow H_2O_2$ is suppressed. Additionally, the number of chloride ions per cubic centimeter in 150 mM NaCl solution is $\approx 9 \times 10^{19} cm^{-3}$. This is almost $10^{4-5} cm^{-3}$ higher than the concentration of hydroxyl radicals that could be present at the plasma–liquid interface (concentration of hydroxyl radicals at plasma–liquid interface for a similar setup $= 10^{14-15}\ cm^{-3}$ [19]). For APPJ in contact with DIW and NaCl solution, although $^{\bullet}OH$ are generated at similar rates, the presence of high chloride concentrations in NaCl solutions causes rapid $^{\bullet}OH$ scavenging that suppresses $^{\bullet}OH$ recombination and limits OH-mediated NO_2^- formation

(pseudo-first order kinetics). In contrast, the absence of such scavengers in DIW allows •OH radicals to persist and recombine, resulting in higher concentrations of H_2O_2 and NO_2^-.

The reactive chlorine species formed through reactions (15)–(19) thus result in the higher absorbance of the KI-starch solution in figure 10. HOCl is a stronger and more reactive oxidative agent (than H_2O_2 and NO_2^-) and this also results in stronger color change of the KI-starch-gel in figure 9. Some prior studies also conducted a measurement of the absorbance spectra of the hypochlorite solution in potassium iodide solution and the absorption as observed in our current study (≈400–650 nm) matches with those observations [38, 39] suggesting HOCl is formed in our experiments.

Additionally, a slightly higher pH for the APPJ treated NaCl solution (figure 8) is attributed to the scavenging of protons (H^+) by $HOCl^-$ intermediates, as described in reaction (15). This proton-consuming mechanism effectively competes with the formation of acidic species, shifting the chemical equilibrium towards a more basic side [40].

Understanding how APPJs interact with liquids of differing electrical properties is essential for advancing both fundamental plasma science and biomedical applications. Non-conductive liquids such as DIW provide a simplified platform for isolating intrinsic plasma–liquid interaction mechanisms, whereas conductive liquids such as saline solutions more closely resemble the physicochemical environment of biological tissues. In this study, 150 mM NaCl solution was employed as a representative conductive medium to systematically probe how the ionic concentration influences plasma characteristics and downstream liquid-phase chemistry. In real physiological fluids, the electrolyte balance is maintained not only by sodium salts but also by significant concentrations of potassium, calcium, and magnesium ions. The presence of dissolved ions modifies interfacial electric fields, affects charge transfer and current pathways, and strongly shapes the fate of plasma-generated reactive species in the liquid phase.

By bridging the gap between simplified model liquids and biologically relevant ionic environments, this work offers a framework for interpreting plasma–tissue interactions with greater realism. Such insights can help guide the rational design of plasma sources and treatment protocols that more precisely control the production and delivery of reactive species in complex biological media. Ultimately, this approach has the potential to move plasma medicine beyond empirical optimization towards a more predictive, mechanism-driven discipline.

4. Conclusions

In this study, we investigated the characteristics of an APPJ and the plasma-induced liquid chemistry during its interaction with saline (150 mM NaCl solution) and non-saline (DIW) medium. Plasma discharge in contact with NaCl solution resulted in the higher charge/current flow towards the target. This resulted in stronger emission from excited species at the plasma–liquid interface, and was confirmed through optical emission spectroscope. The absolute concentration of long-lived RONS (mainly H_2O_2 and NO_2^-), as well as higher absorbance in the UV–Vis spectrum measured for the plasma treated DIW solution directly correlated to the absolute emission intensities of excited species (such as hydroxyl radical, nitrogen second positive system, etc) measured at the plasma–liquid interface through optical emission spectroscopy. However, this was not true for the APPJ interacting with NaCl solution. During the interaction of APPJ with chloride containing solutions, the reaction dynamics shifts towards the formation of HOCl as the rate coefficients of the hydroxyl radical recombining with chloride ions are faster than the two hydroxyl radicals combining to form hydrogen peroxide. Formation of HOCl in plasma activated NaCl solution results in the stronger color change of the KI-starch-agarose gel as well as higher absorbance of the KI solution in the UV–Vis spectrum. Our observations provide strong evidence on the formation of HOCl during plasma treatments of physiological fluids. UV–Vis absorbance and concentrations of H_2O_2 and NO_2^- do not necessarily reflect the true oxidative and biological reactivity of PAW, particularly in chloride-containing systems.

Acknowledgements

Bhagirath Ghimire would like to thank (a) Kwangwoon University (Department of Electrical and Biological Physics)/Plasma Bioscience Research Center at Seoul, South Korea, (b) Lancaster University (Department of Chemistry and Material Science Institute), (c) The University of Alabama in Huntsville, Department of Mechanical and Aerospace Engineering, and the (then) funding agencies for providing with the opportunity to complete this research work. This work was supported by EPSRC EP/V00462X/1 (UK) and NSF EPSCoR RII-Track-1 Cooperative Agreement OIA-2148653 (USA).

Data availability statement

All data that support the findings of this study are included within the article (and any supplementary files).

ORCID iDs

Bhagirath Ghimire 0000-0002-5243-8528
Sushil K K C 0000-0001-5717-2557
Pradeep Lamichhane 0000-0002-4467-0490
Nishtha Gaur 0000-0003-2756-6963
Jun-Seok Oh 0000-0003-3227-8544
Kunning G Xu 0000-0002-1249-0380
Endre J Szili 0000-0002-5165-1490
Robert D Short 0000-0001-9173-1180
Eun Ha Choi 0000-0001-5385-1878

References

[1] Lu X and Ostrikov K 2018 Guided ionization waves: the physics of repeatability *Appl. Phys. Rev.* **5** 031102
[2] Kaushik N K *et al* 2018 Biological and medical applications of plasma-activated media, water and solutions *Biol. Chem.* **400** 39–62
[3] Kc S K, Ghimire B, Hong S-H, Oh J-S and Szili E J 2015 How to control the plasma jet production of reactive species for medical therapy? A topical review *J. Appl. Phys.* **58** 143006
[4] Lu X, Naidis G V, Laroussi M, Reuter S, Graves D B and Ostrikov K 2016 Reactive species in non-equilibrium atmospheric-pressure plasmas: generation, transport and biological effects *Phys. Rep.* **630** 1–84
[5] Kelly S and Turner M M 2014 Generation of reactive species by an atmospheric pressure plasma jet *Plasma Sources Sci. Technol.* **23** 065013
[6] Kim S and Kim C-H 2021 Applications of plasma-activated liquid in the medical field *Biomedicines* **9** 1700
[7] Weltmann K D, Kindel E, von Woedtke T, hahnel M, Stieber M and Brandenburg R 2010 Atmospheric-pressure plasma sources: prospective tools for plasma medicine *Pure Appl. Chem.* **82** 1223
[8] Khlyustova A, Labay C, Machala Z, Ginebra M-P and Canal C 2019 Important parameters in plasma jets for the production of RONS in liquids for plasma medicine: a brief review *Front. Chem. Sci. Eng.* **13** 238–52
[9] Norberg S A, Tian W, Johnsen E and Kushner M J 2014 Atmospheric pressure plasma jets interacting with liquid covered tissue: touching and not-touching the liquid *J. Phys. D: Appl. Phys.* **47** 475203
[10] Stapelmann K, Gershman S and Miller V 2024 Plasma-liquid interactions in the presence of organic matter-A perspective *J. Appl. Phys.* **135** 160901
[11] Bruggeman P J *et al* 2016 Plasma-liquid interactions: a review and roadmap *Plasma Sources Sci. Technol.* **25** 053002
[12] Wende K *et al* 2015 Identification of the biologically active liquid chemistry induced by a nonthermal atmospheric pressure plasma jet *Biointerphases* **10** 029518
[13] Hathaway H, Patenall B, Thet N, Sedgwick A, Williams G, Jenkins T, Allinson S and Short R 2019 Delivery and quantification of hydrogen peroxide generated via cold atmospheric pressure plasma through biological material *J. Phys. D: Appl. Phys.* **52** 505203
[14] Melo T, Rocha L C, Silva R P, Pessoa R S, Negreiros A M P, Sales R, Tavares M B and Alves C 2022 Plasma-saline water interaction: a systematic review *Materials* **15** 4854
[15] Jirasek V and Lukes P 2019 Formation of reactive chlorine species in saline solution treated by non-equilibrium atmospheric pressure He/O_2 plasma jet *Plasma Sources Sci. Technol.* **28** 035015
[16] Baik K Y, Kim Y H, Ryu Y H, Kwon H S, Park G, Uhm H S and Choi E H 2013 Feeding-gas effects of plasma jets on *Escherichia coli* in physiological solutions *Plasma Process. Polym.* **10** 235
[17] Nie L, Duan J, Sun F, Lu X and He G 2018 Effect of tissue thickness and liquid composition on the penetration of long-lifetime reactive oxygen and nitrogen species (RONS) generated by a plasma jet *J. Phys. D: Appl. Phys.* **51** 345204
[18] Zhao Y-M, Ojha S, Burgess C M, Sun D-W and Tiwari B K 2020 Influence of various fish constituents on inactivation efficacy of plasma-activated water *Int. J. Food Sci. Technol.* **55** 2630
[19] Ghimire B, Sornsakdanuphap J, Hong Y J, Uhm H S, Weltmann K-D and Choi E H 2017 The effect of the gap distance between an atmospheric-pressure plasma jet nozzle and liquid surface on OH and N_2 species concentrations *Phys. Plasmas* **18** 073502
[20] Jeon G, Kim C, Cho U M, Hwang E T, Hwang H S and Min J 2021 Melanin-decolorizing activity of antioxidant enzymes, glutathione peroxidase, thiol peroxidase and catalase *Mol. Biotechnol.* **63** 150–5
[21] Veerana M, Kim H-C, Mitra S, Adhikari B C, Park G, Huh S, Kim S-J and Kim Y 2021 Analysis of the effects of Cu-MOFs on fungal cell inactivation *RSC Adv.* **11** 1057
[22] Ghimire B, Szili E J, Lamichhane P, Short R D, Lim J S, Attri P, Masur K, Weltmann K D, Hong S H and Choi E H 2019 The role of UV photolysis and molecular transport in the generation of reactive species in a tissue model with a cold atmospheric pressure plasma jet *Appl. Phys. Lett.* **114** 093701
[23] Sarani A, Nikiforov A Y and Leys C 2010 Atmospheric pressure plasma jet in Ar and Ar/H_2O mixtures: optical emission spectroscopy and temperature measurements *Phys. Plasmas* **17** 063504
[24] Ghimire B, Lamichhane P, Lim J S, Min B, Paneru R, Weltmann K-D and Choi E H 2019 An atmospheric pressure plasma jet operated by injecting natural air *Appl. Phys. Lett.* **113** 194101
[25] Ghimire B, Briggs E F, Sysoeva T A, Mayo J A and Xu K G 2023 Contrasting the characteristics of atmospheric pressure plasma jets operated with single and double dielectric material: physicochemical characteristics and application to bacterial killing *J. Appl. Phys.* **56** 085205

[26] Gazeli K, Noel C, Clément T, Daugé C, Svarnas P and Belmonte T 2013 Multiple solutions in the theory of DC glow discharges *Plasma Sources Sci. Technol.* **22** 025020
[27] Vorac J, Kusyn L and Synek P 2019 Deducing rotational quantum-state distributions from overlapping molecular spectra *Rev. Sci. Instrum.* **19** 123102
[28] Vorac J, Synek P, Prochazka V and Hoder T 2017 State-by-state emission spectra fitting for non-equilibrium plasmas: OH spectra of surface barrier discharge at argon/water interface *J. Phys. D: Appl. Phys.* **50** 294002
[29] Vorac J Synek P, Potocnakova L, Hnilica J and Kudrle V 2017 Batch processing of overlapping molecular spectra as a tool for spatio-temporal diagnostics of power modulated microwave plasma jet *Plasma Sources Sci. Technol.* **30** 025010
[30] Pei X, Lu Y, Wu S, Xiong Q and Lu X 2013 A study on the temporally and spatially resolved OH radical distribution of a room-temperature atmospheric-pressure plasma jet by laser-induced fluorescence imaging *Plasma Sources Sci. Technol.* **22** 025023
[31] Li L, Nikiforov A, Xiong Q, Britun N, Snyders R, Lu X and Leys C 2013 OH radicals distribution in an Ar-H_2O atmospheric plasma jet *Phys. Plasmas* **20** 093502
[32] Srivastava N and Wang C 2011 Effects of water addition on OH radical generation and plasma properties in an atmospheric argon microwave plasma jet *J. Appl. Phys.* **110** 053304
[33] Attri P, Kim Y H, Park D H, Park J H, Uhm H S, Kim K-N, Fridman A and Choi E H 2015 Generation mechanism of hydroxyl radical species and its lifetime prediction during the plasma-initiated ultraviolet (UV) photolysis *Sci. Rep.* **5** 1–8
[34] Uhm H S 2015 Generation of various radicals in nitrogen plasma and their behavior in media *Phys. Plasmas* **22** 123506
[35] Lukes P, Dolezalova E, Sisrova I and Clupek M 2014 Aqueous-phase chemistry and bactericidal effects from an air discharge plasma in contact with water: evidence for the formation of peroxynitrite through a pseudo-second-order post-discharge reaction of H_2O_2 and HNO_2 *Plasma Sources Sci. Technol.* **23** 015019
[36] Ikawa S, Tani A, Nakashima Y and Kitano K 2016 Physicochemical properties of bactericidal plasma-treated water *J. Phys. D: Appl. Phys.* **49** 425401
[37] Tachibana K and Yasuoka K 2020 Understanding of chemical reactions induced by argon plasma in contact with sodium halide solutions: importance of surface properties for plasma-liquid interactions *J. Phys. D: Appl. Phys.* **52** 125203
[38] Zhang Y-Y, Chen X-Z, Liu X-Y, Zhang X-Y, Gao G, Hou S-C and Wang H-M 2019 A highly selective and ultrafast near-infrared fluorescent turn-on and colorimetric probe for hypochlorite in living cells *Anal. Chim. Acta* **1078** 135–41
[39] Yuan L, Lin W, Xie Y, Chen B and Song J 2012 Fluorescent detection of hypochlorous acid from turn-on to FRET-based ratiometry by a HOCl-mediated cyclization reaction *Anal. Chim. Acta* **18** 2700–6
[40] Jirasek V and Lukes P 2023 Efficient oxidation of saline by atmospheric pressure plasma jet operating with He/O_2 gas flow *25th Int. Symp. Plasma Chemistry (ISPC25)*